The neural tissue around SU-8 implants: A quantitative in vivo biocompatibility study

Gergely Márton[a,b,c], Estilla Zsófia Tóth[a,d], Lucia Wittner[a,b,e], Richárd Fiáth[a,b], Domonkos Pinke[b], Gábor Orbán[a,c], Domokos Meszéna[a,b], Ildikó Pál[a,1], Edit Lelle Győri[a,b,e], Zsófia Bereczki[f], Ágnes Kandrács[a,b], Katharina T. Hofer[a,b,2], Anita Pongrácz[b,g], István Ulbert[a,b,e], Kinga Tóth[a,*]

[a] Institute of Cognitive Neuroscience and Psychology, Research Centre for Natural Sciences, Magyar tudósok körútja 2, Budapest 1117, Hungary
[b] Faculty of Information Technology and Bionics, Pázmány Péter Catholic University, Práter utca 50/A, Budapest 1083, Hungary
[c] Doctoral School on Materials Sciences and Technologies, Óbuda University, Bécsi út 96/b, Budapest 1034, Hungary
[d] János Szentágothai Doctoral School of Neurosciences, Semmelweis University, Üllői út 26, Budapest 1085, Hungary
[e] National Institute of Clinical Neuroscience, Amerikai út 57, Budapest, Hungary, 1145
[f] Department of Control Engineering and Information Technology, Budapest University of Technology and Economics, Magyar tudósok körútja 2, Budapest 1117, Hungary
[g] Institute of Technical Physics and Materials Science, Centre for Energy Research, Konkoly Thege Miklós út 29-33, Budapest 1121, Hungary

ARTICLE INFO

ABSTRACT

The use of SU-8 material in the production of neural sensors has grown recently. Despite its widespread application, a detailed systematic quantitative analysis concerning its biocompatibility in the central nervous system is lacking. In this immunohistochemical study, we quantified the neuronal preservation and the severity of astrogliosis around SU-8 devices implanted in the neocortex of rats, after a 2 months survival.

We found that the density of neurons significantly decreased up to a distance of 20 μm from the implant, with an averaged density decrease to 24 ± 28% of the control. At 20 to 40 μm distance from the implant, the majority of the neurons was preserved (74 ± 39% of the control) and starting from 40 μm distance from the implant, the neuron density was control-like. The density of synaptic contacts – examined at the electron microscopic level – decreased in the close vicinity of the implant, but it recovered to the control level as close as 24 μm from the implant track. The intensity of the astroglial staining significantly increased compared to the control region, up to 560 μm and 480 μm distance from the track in the superficial and deep layers of the neocortex, respectively. Electron microscopic examination revealed that the thickness of the glial scar was around 5–10 μm thin, and the ratio of glial processes in the neuropil was not more than 16% up to a distance of 12 μm from the implant.

Our data suggest that neuronal survival is affected only in a very small area around the implant. The glial scar surrounding the implant is thin, and the presence of glial elements is low in the neuropil, although the signs of astrogliosis could be observed up to about 500 μm from the track. Subsequently, the biocompatibility of the SU-8 material is high. Due to its low cost fabrication and more flexible nature, SU-8 based devices may offer a promising approach to experimental and clinical applications in the future.

1. Introduction

Out of several electrophysiological techniques, electrodes implanted directly into the neural tissue allow the monitoring of brain activity with the highest spatial and temporal resolution [1–4]. Sensors in the extracellular space can detect not only local field potentials, but single

and multiunit activity of nearby neurons as well [5]. Compared to single electrodes, high density microelectrode arrays (MEAs) can provide recordings with vastly increased information content, allowing e.g. current source density analysis [6,7] and the development of robust brain-computer interfaces [8]. The utilization of microelectromechanical systems (MEMS) technology enables the construction of such MEAs with high precision, reproducibility and yield.

The majority of such neural MEAs are silicon-based. Related materials, such as Si, SiO_2, Si_3N_4 and noble metals are non-toxic and inert [9,10]. However, the stiffness of silicon, in contrast to the flexibility of the neural tissue, is not advantageous in terms of long-term performance. Implants made of flexible materials provide smoother coupling with the soft tissue, they can follow small motions and pulsations of the brain [11]. This results in a less harsh immune response and more moderate glial scar formation around the electrodes [12,13].

Several types of polymers have been utilized as substrate or insulation materials for neural implants. The most common choices are polyimide, polydimethylsiloxane, parylene and SU-8 [12], but successful neurophysiological experiments were carried out with other types of polymers as well, such as liquid crystal polymers [14], acrylate and thiol-ene-acrylate shape memory polymers [15], etc.

In this study, we examined SU-8, which is an excellent negative photoresist, allowing convenient, rapid and cost-effective microfabrication [16,17]. The SU-8 resist contains SU-8 monomers, dissolved in an organic solvent (originally gammabutyrolacetone, which is replaced by cyclopentone in SU-8 2000 and 3000 [18]) and triarylsulfonium hexafluoroantimonate salt, which acts as a photoacid generator (PAG). The PAG is decomposed and photoacid is generated upon UV exposure. The exposure is followed by a postexposure bake, during which the acid catalyzes polymerization of the SU-8 monomers.

There is a huge potential in utilizing SU-8 for constructing biomedical sensors due to its thermal stability, chemical inertness, fine feature resolution, high aspect ratio and high cross-linking propensity, which reduces the solvent-induced swelling typically associated with negative resists [18]. The polymer has been employed for in vitro electrophysiological applications [19]. In vivo, nerve action potential signals were recorded with SU-8 based microelectrodes within peripheral biodegradable nerve regeneration guide tubes [20]. The polymer was utilized for creating probes, which were used to perform measurements in the rat brain e.g. in the cerebellar molecular layer [21] and on the neocortical surface [22]. The polymer was used as packaging material for a fully integrated minimally invasive wireless neurostimulator [20]. SU-8 microelectrode arrays integrated with microfluidic channels were also constructed [23,24]. Furthermore, the polymer is highly transparent, making it suitable for functioning as a waveguide [25], and can thus be utilized for creating actuators for optogenetic experiments [26].

The question whether SU-8 is biocompatible is not trivial, mainly due to the antimony salt content of its PAG component. One study compared cell proliferation on plasma-treated and untreated SU-8 surfaces [27]. The authors suggested that plasma treatment enriches the antimony on the surface, which should result in decreased viability. In contrast with this, the treatment enhanced cell proliferation, probably due to an increased wettability. Another study with cell cultures found that neurons died when cultured in a media source contacting untreated SU-8 2000 [28]. The authors suggested that this is due to toxic leachates from SU-8. They also offer solutions to improve SU-8 cytocompatibility, such as heat treatment, isopropanol sonication, parylene coating and oxygen plasma treatment. An in vitro study characterized SU-8 leachates, showing that antimony leaching is minimal and is below the recommendations of the United States Environmental Protection Agency under normal physiological conditions [29]. As a part of an ISO 10993 test, SU-8 samples have been implanted into rabbit muscle, for periods of 1 and 12 weeks. The test concluded that SU-8 is non-irritant [10]. Two studies in which researchers characterized the effect of SU-8 implantation subcutaneously showed good biocompatibility, with minimal interaction with the host tissue [29,30].

Most, yet not all of these examples from the literature indicate the biocompatible nature of SU-8. However, despite the widespread use of the polymer as a substrate material of neural sensors, studies investigating the biocompatibility of SU-8 in the central nervous system (CNS) are sparse. Promising results were provided by Fernandez and colleagues in acute experiments, showing that due to its flexibility the mechanical damage caused by SU-8 needles in the rat's brain during its insertion is lower than the one caused by rigid needles [24]. Huang and colleagues in their 2014 paper presented promising MAPII neuronal- and GFAP astroglial-staining in 2-week-long chronic implantations in two rats [31], but without quantitative evaluation. Similarly, only qualitative data were shown by Liu and colleagues, who demonstrated, that SU-8-based mesh electronics injected into the brains of mice exhibit little chronic immunoreactivity and can reliably monitor brain activity [32].

To our best knowledge, no systematic, quantitative study has been performed yet, which might give insight into the biocompatibility of SU-8 in long-term applications within the CNS. Our work addresses this issue by implanting SU-8 3000 probes chronically into the rat CNS for 8 weeks, and by examining the tissue surrounding the implants. We examined the neuronal preservation and the severity of astrogliosis around SU-8 devices implanted in the neocortex of 21 rats, with the aid of immunohistochemical stainings against neurons and glial cells. The quantitative evaluation covers not only a light microscopic examination of the samples, but also a detailed ultrastructural examination of the implanted tissue at the electron microscopic level as well.

2. Materials and methods

2.1. Design and microfabrication of SU-8 implants

The SU-8 implants (probes without electrodes) were designed as follows: 4-inch silicon wafers were used as handling substrates for the construction of the polymer structures. SU-8 3025 (MicroChem Corp., Newton, MA, USA) was spun onto the substrates in two steps at 4000 rpm. Each step formed a 22.5 µm thick layer, thus a total thickness of 45 µm was achieved. The layout of the probes was transferred into the photoresist via standard UV photolithography using photomasks of 1 µm resolution. The last step of this process is a 30 min hard bake at 150 °C. The realized MEMS devices (Fig. 1A) were immersed into distilled water and peeled off by hand from the silicon wafers with a pair of tweezers. No further post processing was applied on the devices before sterilization, which is described in a following section titled "Implantation procedures".

SU-8 implants were designed to contain a 3 mm × 3 mm base regions for handling. Each implant had a single, 5 mm long, 300 µm wide shaft, ending in a tip with an opening angle of 18° (Fig. 1B). The thickness was designed to be 45 µm everywhere, except for a small well on the probe shaft, which might be suitable for containing bioactive matrices in future experiments [33]. The oval pattern on Fig. 1B corresponds to this small well. This feature was not utilized in this study.

2.2. Implantation procedures

In vivo, chronic implantations were performed on 31 Wistar rats (weight range: 220–500 g, 15 female and 16 male). The animals were implanted for two months. In order to reduce the number of animals used, we did not use a separate control group (i.e. animals which were not implanted). Instead of this, we followed a methodology, which is more often used in biocompatibility studies [5,34–38] namely, we compared the device-tissue interface to a non-affected region in a higher distance from the device track (for details see section "2.4. Processing of brain section images").

Animals were kept and handled in accordance with the European Council Directive of 24 November 1986 (86/609/EEC), the Hungarian Animal Act, 1998 and the Animal Care Regulations of the Research
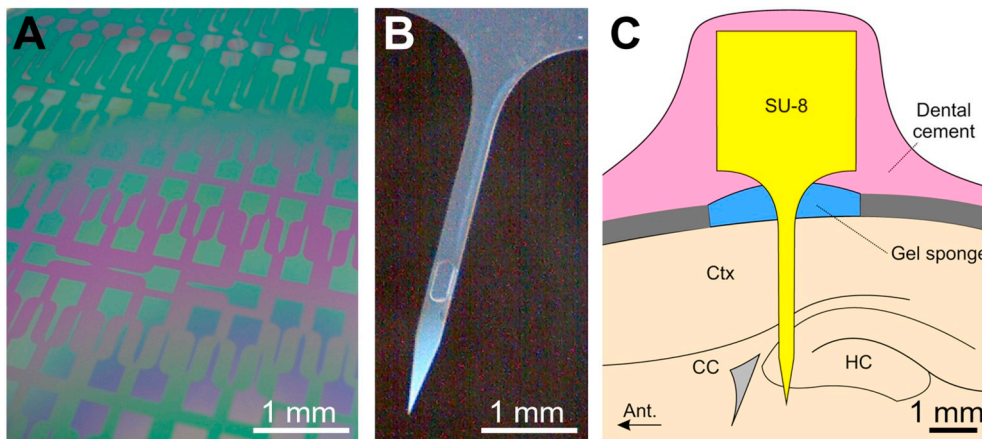
Fig. 1. A: SU-8 devices fabricated with high yield on silicon-wafers as handling substrates. B: Each implant had a 5 mm long, 300 μm wide and 45 μm thick shaft ending in a tip. C: Schematic drawing of implantation, shown in the sagittal plane (medial-lateral 3 mm in reference to the bregma). HC: hippocampus, Ctx: cortex, CC: corpus callosum. The arrow points towards the anterior direction. Each probe had a 3 mm × 3 mm base region served for handling.

Centre for Natural Sciences (RCNS).

The animals were initially anesthetized via intraperitoneal injection of ketamine-xylazine solution (37.5 mg/ml and 5 mg/ml, respectively at 0.2 ml/100 g body weight) and prepared for stereotaxic operation as described elsewhere [39]. The depth of the anesthesia was maintained using intramuscular updates of the same solution (0.3 ml/h). A body temperature of 37 °C was sustained with the aid of an electric heating pad connected to a temperature controller (Supertech, Pécs, Hungary). During anesthesia, paraffin oil (Hungaropharma, Budapest, Hungary) was administered to the eyes to prevent drying.

The probes were sterilized before implantation by immersing it in 70% ethanol for 5 min, followed by washing it with a continuous stream of distilled water for 2 min. In order to reduce the number of animals used, the SU-8 probes were implanted into both hemispheres of each animal, at the anterior-posterior (AP)-3 mm, medial-lateral (ML) 3 mm coordinates in reference to the bregma, as shown in Fig. 1C. The craniotomy had been performed at the implant locations in such a manner that a 2.5 mm (AP) x 3 mm (ML) wide window was drilled into the skull above each hemisphere, centered at the implant target locations. A slight section on the dura was made at the places of implantation. A stereotaxic frame with manipulators (David Kopf Instruments, Tujunga, CA, USA) was employed for implantation, during which the plane of the SU-8 structure was approximately parallel to the sagittal plane. In some cases, a minor (<0.2 mm) deviation from the target location was utilized in order to avoid visible, large blood vessels. The implantation depth was 4 mm. The craniotomy window was closed with gel sponge (Gelaspon, Ankerwerk, Rudolstadt, Deutschland) and the implants were covered with dental cement (Vertex cold-curing acrylic denture repair material, Vertex, Soesterberg, The Netherlands) in order to prevent contamination.

2.3. Perfusion and histology

After eight weeks, the animals were deeply anesthetized with a high dose of ketamine/xylazine (73 mg/kg and 10 mg/kg, respectively) and transcardially perfused first with physiological saline (3 min), then with a fixative containing 4% paraformaldehyde and 15% picric acid in 0.1 M phosphate buffer (pH = 7.4, 300 ml). The fixed brain was taken out of the skull and the implanted devices were gently removed from the brain. 60-μm-thick horizontal sections were cut from the brain and processed for immunohistochemistry.

Neuronal Nuclei-immunostaining (NeuN, Millipore, clone A60, 1:2000) was used for visualization of neuronal cell bodies and Glial Fibrillary Acidic Protein-immunostaining (GFAP, Millipore, clone GA5, 1:2000) was used for labeling glial cells. For more details see Fiath et al. 2018 [5].

The immunostained sections were dehydrated either for light microscopy or electron microscopy. In the former case sections were

mounted, treated with xylene (2 × 10 min) and cover-slipped with DePex (Serva). In the latter case, sections were treated with 0.5% OsO₄ in phosphate buffer for 30 min, dehydrated in ethanol and mounted in Durcupan (Sigma).

After light microscopic examination, areas of interest were re-embedded and sectioned for electron microscopy. Ultrathin serial sections were collected on Formvar-coated single slot grids, stained with lead citrate, and examined with a Hitachi 7100 electron microscope.

2.4. Processing of brain section images

21 animals (42 probe tracks) were included in the qualitative analysis out of the 31 implanted. Three animals died right after the surgery and in case of seven animals the probe was fell off a few days after the implantation, probably due to a suboptimal fixing to the skull.

All 42 samples were examined at the light microscopic level (Table 1). The probe tracks were identified and photographed at 2.5-, 5- and 10-fold magnification in all sections of each sample. Heading from the pial surface of the brain towards the white matter, every sixth section was labelled for GFAP, all the others were stained for NeuN.

The quantitative analysis of the NeuN- and GFAP-immunostained sections (cell counting and calculation of staining intensity, respectively) was performed using home-made routines, as follows.

2.4.1. NeuN-stained sections

An automated method was developed in Matlab (The MathWorks, Natick, MA, USA), in order to process the large number of images

Table 1
Number of the examined specimens.

	Number of animals	Number of hemispheres	Number of sections	Number of ROIs
Qualitative analysis of the implant track – light microscope				
NeuN-staining	21	42	840	–
GFAP- staining	21	42	154	–
Validation of the automated cell-counting routine – light microscope				
NeuN-staining	6	6	6	24
Quantitative analysis of neuronal preservation – light microscope				
NeuN-staining	18	32	189	441
Quantitative analysis of astroglial reaction – light microscope				
GFAP-staining	12	18	59	194
Quantitative analysis of synaptic density – electron microscope				
NeuN-staining	3	3	3	9
GFAP-staining	2	2	2	6
Quantitative analysis of the ratio of glial processes – electron microscope				
GFAP-staining	3	3	3	9

obtained from brain sections. With a graphical user interface, input images were loaded (Fig. 2A), on which the probe track was manually determined (Fig. 2B). The algorithm circumscribed regions of interests (ROI) in the vicinity of the probe track in four (anterior, posterior, medial, lateral) directions, in accordance with previous studies [34,35] (Fig. 2D). The cell centroids in NeuN-immunostained section images were detected with an algorithm based on the watershed method [40], which allows the discrimination of cell bodies located close to each other. The number of centroids was calculated in 20 μm wide sectors up to a distance of 400 μm from the track, as visible on the generated Matlab figure (Fig. 2A-D). Cell counts and density values were saved in excel files (Supplementary Table 1). The density values of each sector were normalized to the average values of the 200 to 400 μm region. This value will be called normalized neuron density. The 200 to 400 μm region was regarded as control region. Note, that no separate control group of non-implanted animals were used.

An additional capability of our home written program is the possibility to define a region for manual counting (Fig. 2C). The importance of this feature is that a darker background staining was often observed in the tissue around the track, interfering with the automated cell counting. The darker background staining usually resulted from the differences in the diffusion of the immunohistochemical antibodies in liquid vs. in brain tissue. The penetration of the antibody into the tissue was the best on the surfaces of the free-floating tissue sections. The device track, which composed a third, perpendicular surface to the lower and upper surface of the section sample provided an extra, well stained surface, resulting in a darker background when observed in the light microscope.

Sixty μm thick tissue samples (examined with a light microscope) will be referred to as sections throughout the whole article. Areas in which analyzes of cell counts, intensity of glial staining, synaptic density or density of glial elements were performed will be referred to as ROIs. Subareas of ROIs determined as a function of the distance from the implant track will be called sectors.

2.4.2. Validation of the automated cell-counting routine

The reliability of the automatized cell counting was tested in six randomly chosen NeuN-stained sections deriving from six different animals. Systematic statistical comparison was made between manual and software-based counts. Since the observations from the two datasets were paired, a nonparametric Wilcoxon signed rank test was used to test their difference. Calculations were performed by using Matlab built-in routines.

Comparison of the two datasets was performed as follows: We outlined four areas (ROIs) in the vicinity of each implant track (in all four directions), up to a distance of 400 μm from the border of the track, and divided them into twenty equally long sectors (see Fig. 2D). For each sector, the number of neurons was determined both with manual and software-based counting. After finishing the calculations for individual tracks, the sectors corresponding to the same distance from the implant track were averaged. This averaging resulted in two tables with 4 columns (anterior, posterior, medial, lateral) and 20 rows (sectors) containing averaged cell counts for both manual and software-based counting. Normalized neuron density was determined for each sector. Wilcoxon signed rank test was applied on this averaged table. There was no significant difference between the manual and software-based counting method at $p = 0.05$. P-values are the following: $p = 0.1855$ (lateral), $p = 0.1797$ (anterior), $p = 0.598$ (medial), $p = 0.4531$ (posterior).

2.4.3. GFAP-stained sections

The graphical user interface also allowed a manual determination of the probe track, which was used on images made from GFAP-immunostained sections. Sectors were determined similar to the NeuN images, except that the width of the sectors was 40 μm (instead of 20 μm) and the examined distance was 800 μm (instead of 400 μm), because of the more widespread nature of the glial reaction. In this case, however, the average pixel intensity of the sectors was calculated, which is a commonly used protocol to determine the extent of the glial response around the implant [34,35]. The intensity values were saved in Excel files and were normalized to the average values of the 600 to 800 μm region, which was regarded as control region. Note, that no separate control group of non-implanted animals were used.

As this method was originally developed for fluorescent staining, the intensity values show the brightness of the image pixels. We used non-fluorescent immunostaining (see Fiáth et al. 2018), where immunopositive elements are visualized with a dark brown precipitate of diaminobenzidine. Darker staining represents higher immunopositivity, therefore lower pixel intensities indicate higher densities of GFAP-positive elements.

2.5. Quantitative analysis of the NeuN- and GFAP-immunostained sections

The number of neurons surrounding the implant track was determined on the NeuN-stained sections by the software-based automated method described above. For this analysis, we used 32 probes implanted into 16 left and 16 right hemispheres of 18 animals, and 3–9 (but typically 5–6) sections of each hemisphere were analyzed (Table 1). Care was taken not to analyze neighboring sections, to avoid double sampling of neurons on the surface of the section, cut in half during the slicing procedure. In several cases an injury- or bleeding-caused cell loss was visually identified on one or more sides of the track (or even in the whole sections). These sides and sections were excluded from the analysis, since this type of cell loss was independent of the
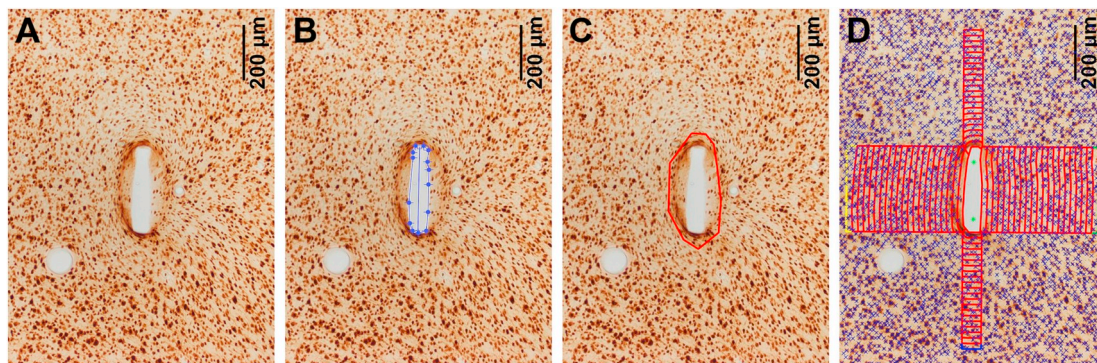

Fig. 2. Process of the automated cell counting. The track outline (B) and the area for manual counting (C) were selected on the loaded image (A) by the user. The program defined 20 μm wide sectors up to 400 μm on the 4 sides of the track starting from the outline. The number of NeuN-positive cells and the area of the sectors were calculated by the program. The results were saved in a Matlab figure (D). The density values of all sectors were then normalized to the average values of the 200 to 400 μm region, regarded as control.

biocompatibility of the probe. Since neuronal densities show high variability in the different cortical layers, only ROIs covering the same cortical layer were analyzed. If a ROI covered layers with different neuron densities (such as layer 4 and layer 5), it was excluded from the analysis, to avoid false results. Altogether 441 ROIs were analyzed in 189 sections.

The amount of gliosis surrounding the implant track was determined on the GFAP-stained sections by the automated method described above. We analyzed 2–4 (but typically 3–4) sections of each track, from probes implanted into 9 left and 9 right hemispheres of 12 animals (Table 1). ROIs containing injury- or bleeding-caused cell loss were excluded from the analysis as mentioned above. Altogether 194 ROIs were analyzed in 59 sections.

2.6. Quantitative electron microscopic analysis

The ultrastructural features of the brain tissue surrounding the implant were examined in the case of 3 samples (2 left and 1 right hemispheres, from 3 different animals) both in NeuN- and in GFAP-stained sections (Table 1). Care was taken to perform the re-embedding in each sample approximately from the same depth of the neocortex.

The density of synaptic contacts was analyzed as a function of the distance from the track both in the NeuN- and GFAP-stained tissues. 8 μm wide and 12 μm thick sectors constituting one ROI were defined from the track outline, up to 192 μm distance, in three different locations along the track (Fig. 3). Synaptic contacts were counted manually in each sector. The density of synaptic contacts was determined per 100 μm² area with the Fiji ImageJ program.

The density of the glial elements was analyzed as a function of the distance from the track in the GFAP-stained tissues. 8 μm wide and 12 μm thick sectors, which together constitute one ROI, were defined

Fig. 3. The ultrastructural analysis of the brain tissue surrounding the SU-8 implant was performed at the electron microscopic level. Ultrathin sections (55 nm) were prepared. The density of synaptic contacts and the ratio of glial elements were analyzed as a function of the distance from the track (A). 8 μm wide and 12 μm thick sectors constituting one ROI were defined from the track outline, up to 192 μm distance in three different locations along the track. B shows the magnification of the sectors labelled in white frame in A. Synaptic contacts were counted manually in each sector on high magnification images. The density of synaptic contacts was determined per 100 μm² area using Fiji ImageJ. The area of the glial elements was measured in each sector and was divided by the area of the sector with the aid of the Fiji ImageJ program.

from the track outline, up to 180 μm distance, in three different locations along the track. The area of the glial elements was measured in each sector and was divided by the area of the sector with the aid of the Fiji ImageJ program.

2.7. Statistical analysis

In case of the neuronal density, astroglial staining intensity, density of synapses and density of glial processes the statistical analysis was performed using the Statistica software (StatSoft, Tulsa, OK, USA). Normality of the data sets was tested using the Kolmogorov-Smirnov & Lilliefors tests. Since none of the data followed a normal distribution, the nonparametric Kruskal-Wallis ANOVA test was used. The significance level was set to $p = 0.05$.

In case of the validation of automatic cell counting the statistical analysis was performed using Matlab built-in routines. The nonparametric Wilcoxon signed rank test was used to test the difference of the two data sets (manual versus automated counting). The significance level was set to p = 0.05.

See Table 1 for the sample sizes of the examined specimens.

3. Results

In the present study, we aimed to examine the long-term biocompatibility of SU-8 devices chronically implanted in the rat neocortex. We present histological data on the preservation of neurons surrounding the implant track and on the severity of astrogliosis. We provide a detailed, quantitative evaluation of a large data set applying a home-made routine developed for automated image analysis.

In addition, beside the light microscopic evaluation, we introduce thorough, quantitative electron microscopic analysis on the general ultrastructure and density of synaptic contacts and on the glial processes in the neural tissue near the implant.

3.1. Microfabricated implants

The SU-8 structures were fabricated with high yield (Fig. 1). Each probe had a 3 mm × 3 mm base region for handling and a 5 mm long, 300 μm wide and 45 μm thick penetrating shaft. No electrode contacts were present on the implant shafts. Less than 10% of the probes were damaged, mainly due to tearing while removing them from the wafer. Despite the flexibility of the SU-8 material, the devices were stiff and sharp-edged enough to penetrate the brain once the dura mater was incised.

3.2. Characterization of the implanted brain tissue

3.2.1. Bleeding- and injury-caused tissue damage

Bleedings may occur during the probe insertion by injuring superficial or deeper capillaries. Severe damage was observed in case of 9 hemispheres in 6 animals caused by an intense bleeding. Since serious bleeding did not occur during the probe insertion procedure, we hypothesize that the probe moved in a lateral direction within the brain after the insertion, possibly because the animal hit his head during the 2-months survival period. All sides of the probe were affected by the bleeding, all along the depth of the probe. Both neurons and glial cells were severely damaged or even absent. These hemispheres were excluded from the quantitative analysis. Minor bleedings also occurred, resulting in a smaller damage, which affected only one or two sides of the track and was confined to a subset of the neocortical layers. In these cases, those sides which were unaffected by the bleeding were included in the quantitative analysis, while the affected sides were excluded.

Overall, both serious and minor injuries occurred more frequently in the superficial layers than in the deeper layers. In most cases, regions with neuronal loss caused by bleeding co-occurred with a stronger gliosis on the neighboring GFAP-stained section. There were only two
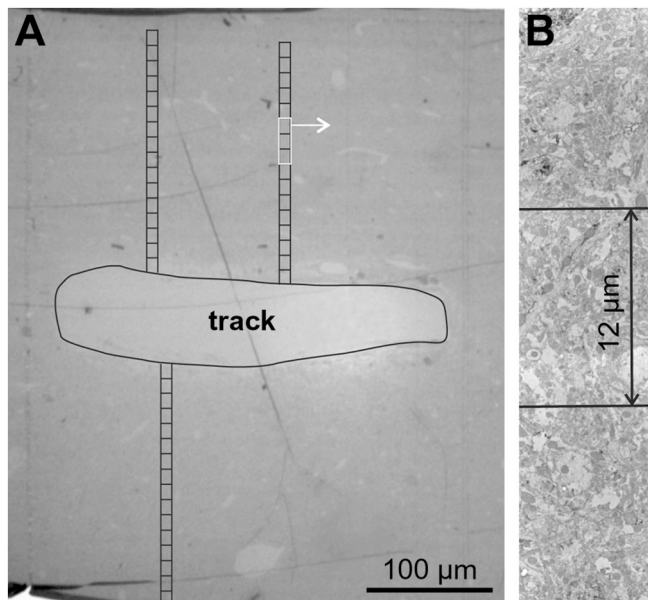
exceptions where the intense cell loss coincided with the loss of GFAP-staining, indicating the loss of glial cells and processes as well.

Taken together, bleeding-caused effects are most probably independent of the biocompatibility of the implant material, therefore brain regions affected by bleeding were excluded from the quantitative analysis.

3.3. Preservation of neurons around the implants

The severity of the neuron loss in the vicinity of the implant was studied in a total of 441 ROIs involving the examination of 189 sections, deriving from 18 animals (see Section 2 Materials and methods, Table 1). The neuronal density was examined as a function of the distance from the implant track. The data were normalized to the 200–400 μm region from the track, which was regarded as control.

As described earlier, the NeuN-immunopositive neuronal cell bodies were distributed throughout the whole neocortex, at different densities in the different layers [41,42]. Low numbers of cells were found in layer 1. Layers 2 and 4 formed very dense and compact layers, with high neuron densities, whereas neurons in layers 3, 5 and 6 were larger and more sparsely distributed, therefore, a lower neuron density was observed in these layers. In contrast to neuron density, the distribution of astroglial cells and their processes were quite uniform among the different layers, with a slightly increasing density towards the white matter [43–45].

We could not find any significant difference in the neuronal survival between the hemispheres (left or right), between the different sides of the track (anterior-posterior-lateral-medial) and between the different depths of the neocortex ($p > 0.05$). Sectors of the same distance were compared in all cases. Data deriving from the two hemispheres, from the four sides of the track and the different neocortical depths were pooled.

Considerable neuronal loss was observed in the first sector (20 μm distance from the side of the penetration track), on average, only 24% of the cells were preserved (normalized average density: 0.24 ± 0.28). There was a significant loss of neurons in the neighboring sector (distance of 20–40 μm) as well, but to a considerably lower degree: approximately 74% of the neurons were preserved (0.74 ± 0.39). From longer distances than 40 μm, the density of neurons was comparable with the control region (200–400 μm) (Fig. 4) (Table 2).

3.4. Astroglial reaction around the implants

The severity of the astroglial reaction in the vicinity of the implant was analyzed in a total of 194 ROIs involving the examination of 59 sections, derived from 12 animals. The intensity of the GFAP-immunostaining was examined as a function of the distance from the implant track.

The astroglial reaction surrounding the implant track was found to be considerably more extended than the neuronal loss. Therefore, we performed the quantitative analysis within a larger radius (800 μm) in the case of the GFAP-stained sections (Fig. 5A-D), compared to the NeuN-positive sections. The area from 600 to 800 μm was regarded as control (Fig. 5E, gray frame). Data derived from other sectors were normalized to GFAP staining intensities found in this region.

Regarding the severity of the astrogliosis surrounding the track, we could not find any difference either between the hemispheres or between the different sides of the track (anterior-posterior-lateral-medial) ($p > 0.05$). Therefore, these data were pooled. However, in contrast to the observations regarding neuronal loss, the severity of the astroglial reaction close to the track showed a difference between the various depths of the neocortex (Fig. 5). Therefore, sections from the superficial and from the deep layers were examined separately. The differentiation between sections from superficial or deep layers was based on the neighboring NeuN-stained sections. Cortical lamina 1–3 were regarded as superficial- whereas lamina 4–6 were regarded as deep layers.

The quantitative examination (i.e. measuring the pixel intensity within the ROIs) confirmed that within 240 μm from the penetration track, the intensity of the GFAP-staining was significantly more intense in the superficial than in the deep layers of the neocortex (Fig. 5E, red dashed frame). As pixel intensity is inversely correlated to immunopositivity (see Section 2. Materials and methods), lower values represent a higher density of immunostained elements. The normalized staining intensity ranged from 0.29 ± 0.14 to 0.81 ± 0.15 in the superficial, whereas from 0.44 ± 0.21 to 0.87 ± 0.17 in the deep layers (significantly different, $p < 0.05$). At a distance larger than 240 μm the intensity of the astroglial reaction showed no difference between the superficial and deep layers, with values ranging from 0.85 ± 0.14 and 0.90 ± 0.15 to 1.01 ± 0.03 and 1.02 ± 0.19 in superficial and deep layers, respectively (for data see Table 3).

With increasing distance from the penetration track, the intensity of the GFAP-staining showed a gradual decline, both in the superficial and deep layers. The astroglial reaction was considerably more extended than the neuronal loss. In case of the superficial layers, we found a significantly increased intensity of astroglial staining up to 560 μm compared to the control region, i.e. the normalized average pixel intensity was significantly different from the control regions in the sectors ranging from 0 to 560 μm distance from the penetration track. The normalized average pixel intensity gradually increased from 0.29 ± 0.14 (in close vicinity to the track) to 0.98 ± 0.06 (at 520–560 μm distance from the track, Fig. 5E, dark blue frame) (see also Table 3). In the deep layers the extent of the increased GFAP-staining was lower than in the superficial layers. We found a significantly increased staining intensity up to 480 μm (Fig. 5E, light blue frame) (see also Table 3). In the deep layers the normalized average pixel intensity gradually increased from 0.44 ± 0.21 (0–40 μm from the track) to 0.99 ± 0.18 (at a distance of 440–480 μm from the track). These values were significantly different from those measured in the control region.

3.5. Results of the electron microscopic analysis

Extracellular electrodes can achieve high quality, biologically relevant electrophysiological signals, if the brain tissue surrounding the electrode contains healthy neurons, healthy dendrites and axons, preserved synaptic contacts and a low level of gliosis [46]. As we described above, we made a quantitative analysis to estimate the number of neurons, and the level of gliosis at light microscopic level, to see how the SU-8 material changes the structure of the brain tissue. Although light microscopic analysis of NeuN-stained sections showed a preservation of neurons in close vicinity of the track, it does not provide any information about the structure of the neuropil, the dendrites, axons and the presence of synaptic contacts. Transmission electron microscopy – due to its high resolution – is suitable to answer these questions at the submicron scale. Therefore, we studied the morphological features of the neurons and their processes at the subcellular level, the general ultrastructure of the neuropil and we quantified the number of the synaptic contacts as a function of the distance from the implant track.

At the light microscopic level, we detected a dense mass of GFAP-immunostained elements close to the implant track. However, within a 60 μm thick section, stained elements which are not in focus can also amplify the darkness of the analyzed picture. The darker staining in close vicinity of the track might thus be partly explained by technical reasons. The penetration of the antibody into the tissue is the best at the liquid-tissue interface of the sections. The "walls" of the implant track, which compose a third, perpendicular surface to the lower and upper surfaces of the section provides an extra, well stained tissue volume. This results in a darker background staining, than the background in areas at higher distances from the track, where this extra surface is lacking. To estimate the impact of this optical phenomenon in the evaluation of the gliosis, we measured the amount of astroglial processes in ultrathin sections at the electron microscopic level as a
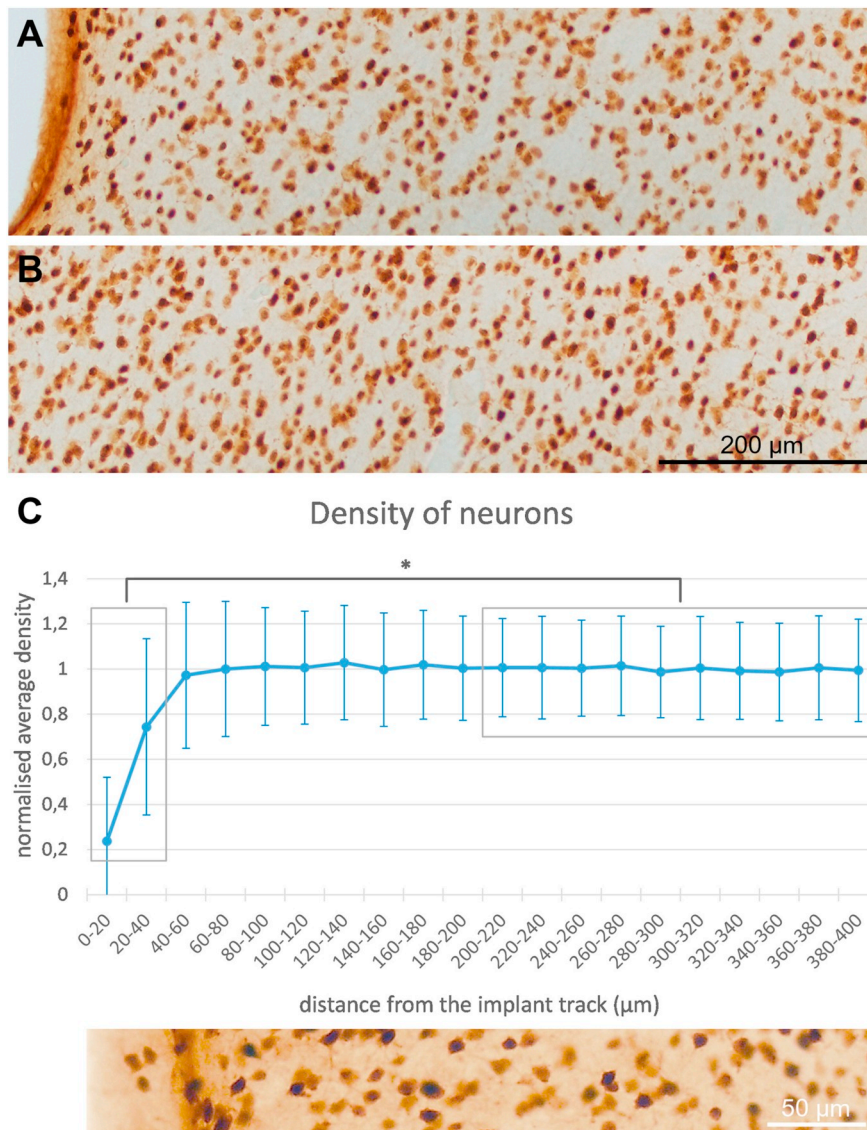
Fig. 4. Preservation of neurons near the SU-8 implant. A-B: Representative images of NeuN-staining. Neuron loss was observed only in the close vicinity of the implant track (A). B shows a reference cell density at a distance of 1 mm. C: Quantification of the neuronal cell loss near the implant. The neuronal density was calculated as a function of the distance from the device track. Data were normalized to the 200–400 μm region, which was regarded as a control. The density of neurons significantly decreased in the first 20 μm: the normalized average density was 0.24 ± 0.28. A lower, but still significant neuron loss in the 20–40 μm sector could also be observed (normalized average density: 0.74 ± 0.39). From a distance of 40 μm the density of neurons was control-like. Bottom figure on C shows an example ROI with a scaling which fit the divisions of the graph. The asterisk (*) labels significant differences ($p < 0.05$) between the first 40 μm and the control region (gray boxes).

Table 2
Neuronal cell counts as a function of the distance from the SU-8 implant. The asterisk (*) labels significant difference compared to the control region (200–400 μm), $p < 0.05$.

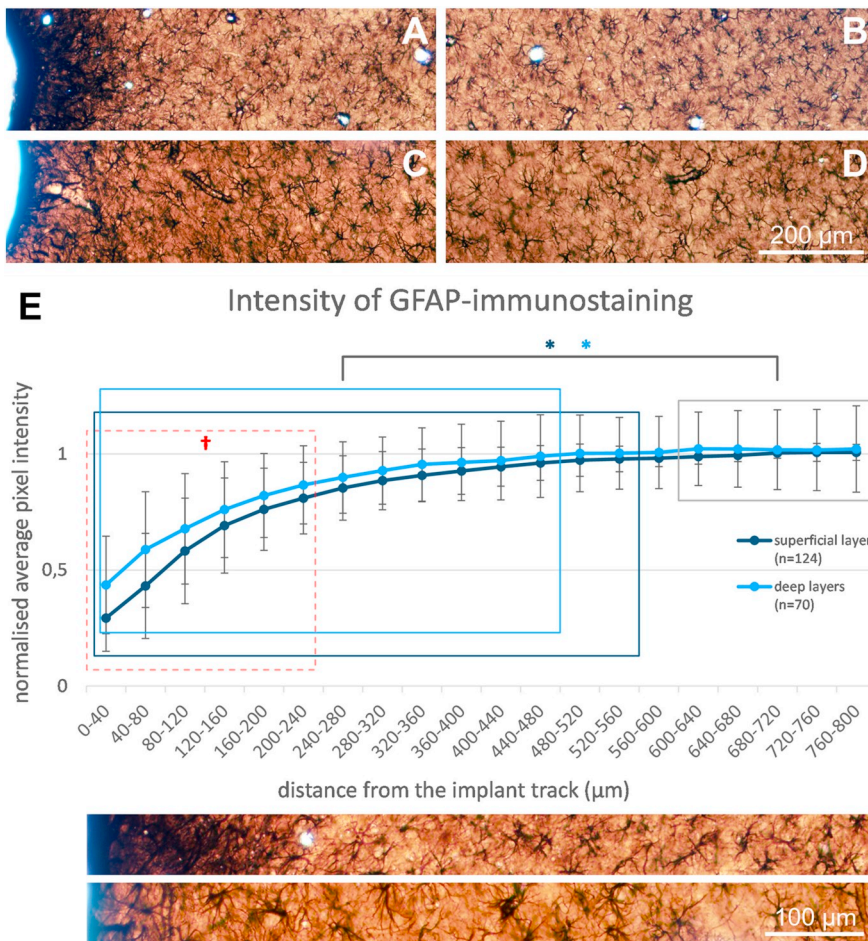| Distance from the track (μm)	Normalized average neuron density	StDev
0–20 *	0.24	0.28
20–40 *	0.74	0.39
40–60	0.97	0.32
60–80	1.00	0.30
80–100	1.01	0.26
100–120	1.00	0.25
120–140	1.03	0.25
140–160	1.00	0.25
160–180	1.02	0.24
180–200	1.00	0.23
200–220	1.01	0.22
220–240	1.01	0.23
240–260	1.00	0.21
260–280	1.01	0.22
280–300	0.99	0.20
300–320	1.00	0.23
320–340	0.99	0.21
340–360	0.99	0.22
360–380	1.01	0.23
380–400	0.99	0.23

function of the distance from the implant track.

3.5.1. General ultrastructure

In all examined samples, a 5–10 μm thin glial scar – formed by glial cells and processes – separated the penetration track from the neural tissue (Fig. 6A, B, arrows). Close to the track, signs of tissue damage were visible as caverns were located in the neuropil. These structures usually had a discontinuous membrane and contained no or few disrupted organelles (white cysts on Fig. 6A, B, D).

In one out of the three examined samples, only a few caverns were visible (Fig. 6A), extending to a distance of ~30 μm from the track. In these regions, NeuN-stained cell bodies were present very close to the track (~10–15 μm, arrowheads). Several of these neurons displayed an oval shape, possibly resulting from the physical compression caused by the probe. In this case a continuous glial scar of ~2–5 μm thickness was surrounding the penetration track. In the two other examined samples, caverns were considerably more frequent, and were spread further than ~50 μm away from the track. The glial scar was ~10–15 μm thin (Fig. 6B). In these samples, healthy, spherical neurons were present at larger distances from the track (~30–40 μm, Fig. 6B, arrowheads). Note that the area covered by caverns was not visible at the light microscopic level.

At distances of ~50–100 μm from the track, several NeuN-positive

Fig. 5. Representative images of GFAP-staining from the upper- (A, B), and lower layers (C, D) of the implanted neocortex. A and C show the vicinity of the injury, B and D show a reference staining at a distance over 1 mm. Both the intensity and the extension of the astroglial reaction close to the track were most enhanced in the upper layers (A), with a gradual decline towards the lower layers (C). The intensity of the staining at distances over 1 mm from the track did not show any difference for different depths of the neocortex (B, D). However, in very close vicinity to the device track a massive glial scar seemed to be present regardless of the depth (A, C).

E: Quantification of the astrogliosis near the SU-8 implant. The intensity of the GFAP-staining was calculated as the function of the distance from the device track. (Higher staining intensity denotes a lower pixel intensity on the y-axis). Data were normalized to the 600–800 μm region, which was regarded as a control (gray box). In the first 240 μm (red dashed frame) the intensity of the GFAP-staining was significantly higher in the superficial layers compared to the deep layers, suggesting a more intense gliosis in these neocortical laminae. At larger distances no difference was found between the various depths of the neocortex. The astroglial reaction was reduced with increasing distance from the implantation site as the rising pixel-intensity values denote. The intensity of the GFAP-staining was significantly enhanced up to 560 μm distance in case of the superficial layers (dark blue frame) and up to 480 μm in case of the deep layers (light blue frame). Note the considerably higher extent of the astroglial reaction compared to the neuronal sensitivity. Bottom figure on E shows example ROIs either from superficial (upper) or from deep layers (lower) with a scaling which fit the divisions of the graph. Cross (†) labels significant difference between superficial and deep layers, p < 0.05. Stars (*) label significant difference compared to the control region (gray box), p < 0.05.

Table 3

Quantitative analysis of the astroglial reaction as a function of the distance from the SU-8 implant. The cross (†) labels significant difference between superficial and deep layers, p < 0.05. The asterisk (*) labels significant difference compared to the control region (600–800 μm), p < 0.05.

Distance from the track (μm)	Normalized average pixel intensity	StDev	Normalized average pixel intensity	StDev
	Superficial layers (n = 124 ROIs)		Deep layers (n = 70 ROIs)	
0–40 †	0.29 *	0.14	0.44 *	0.21
40–80 †	0.43 *	0.23	0.59 *	0.25
80–120 †	0.58 *	0.23	0.68 *	0.24
120–160 †	0.69 *	0.20	0.76 *	0.21
160–200 †	0.76 *	0.18	0.82 *	0.18
200–240 †	0.81 *	0.15	0.87 *	0.17
240–280	0.85 *	0.14	0.90 *	0.15
280–320	0.88 *	0.13	0.93 *	0.14
320–360	0.91 *	0.11	0.96 *	0.16
360–400	0.93 *	0.10	0.96 *	0.16
400–440	0.95 *	0.08	0.97 *	0.17
440–480	0.96 *	0.08	0.99 *	0.18
480–520	0.97 *	0.07	1.00	0.17
520–560	0.98 *	0.06	1.00	0.15
560–600	0.98	0.04	1.01	0.16
600–640	0.99	0.03	1.02	0.16
640–680	0.99	0.03	1.02	0.16
680–720	1.00	0.02	1.02	0.17
720–760	1.01	0.04	1.02	0.18
760–800	1.01	0.03	1.02	0.19

cell bodies could be seen, with round shapes and healthy ultrastructure (Fig. 6C). In these areas, caverns were only occasionally detected. Apart from this, the tissue had a healthy-looking ultrastructure with a large number of neuronal dendrites, axon terminals and synaptic contacts (Fig. 6E).

3.5.2. Synaptic contacts near the implant

The presence of synaptic contacts is essential for neuronal communication. Thus, neurochemical signaling flowing through the synapses fundamentally contributes to the generation of electrical signals detectable by extracellular electrodes. The density of synaptic contacts was measured as a function of the distance from the track to estimate the effect of the SU-8 material on the synaptic connectivity in the tissue surrounding the implanted probe. We counted the number of synapses in sectors located up to a distance of ~190 μm from the border of the penetration track (Fig. 7).

Synaptic contacts were occasionally visible as close as 6–12 μm from the penetration track. The density of the synaptic contacts was significantly lower in the first 12 μm than at larger distances ($6.44 \pm 13.05/100\,\mu m^2$ vs. $36.45 \pm 10.19/100\,\mu m^2$ in sectors of 0–12 μm and 180–192 μm, respectively) (Fig. 7). Between 12 and 24 μm the density was still reduced ($16.01 \pm 13.47/100\,\mu m^2$) compared to the 180–192 μm sector, although the difference was not significant ($p = 0.1150$). From a distance of 24 μm from the track, the number of synapses was comparable with that measured at 192 μm (for values, see Table 4).

Up to ~30 μm distance from the penetration track, a small minority of the synapses was damaged, i.e. the pre- and/or postsynaptic elements
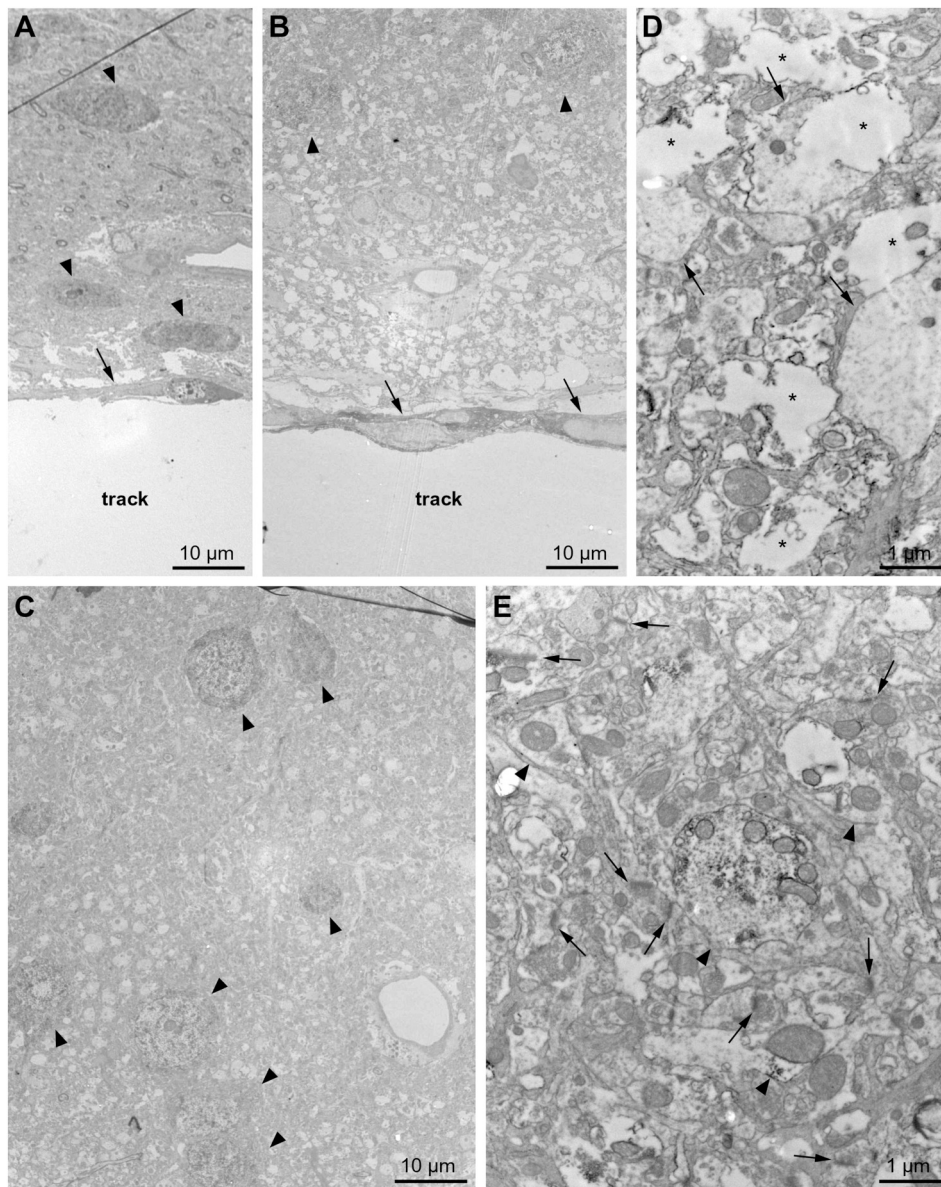
Fig. 6. Low (A, B and C) and high (D, E) magnification electron micrographs of the neocortical tissue surrounding the SU-8 implant. A-B (~0–60 μm): A 5–10 μm thick glial scar was formed of glial cells and processes separating the implant from the brain tissue (arrows). In close vicinity of the track, the tissue displayed different degrees of damage. In some regions (A), only a few caverns indicated the injury of the brain tissue. In these cases, neurons could be observed as close as 10–15 μm (arrowheads) and the glial scar was very thin (A). In other regions (B), the damage was more widespread, large caverns were visible up to 20–40 μm and the first neurons appeared at a distance of approx. 40 μm from the track (arrowheads). In these cases, the glial scar was thicker (B).
C: The figure shows tissue at ~60–145 μm distance from the track. Several NeuN-positive cells could be observed (arrowheads). Some caverns were still visible but in markedly reduced amounts. D (~24–33 μm): High magnification photo of the more intense damage shown in B. Several glial elements could be observed (arrows) and large caverns, often with damaged or incomplete membranes were also visible (asterisk). E: At a larger distance from the track (~70–80 μm) the ultrastructure of the tissue was normal, as many neuronal dendrites (arrowheads) and synapses (arrows) were present.

had incomplete membranes, but the synaptic cleft was always preserved (Fig. 7A-C) [47]. At distances of >60 μm, damaged synaptic contacts were not observed, and pre- and postsynaptic profiles constituting the synapses were intact (Fig. 7D-G).

3.5.3. Glial processes near the implant

An increased density of glial elements was found at the light microscopic level in close vicinity to the penetration track compared to farther distances. As the technical concerns detailed above might (partly) account for this increase, we performed a quantitative analysis of the glial elements at the electron microscopic level to estimate a more precise level of gliosis around the penetration track. Therefore, we determined the ratio of the glial processes within the neuropil, as a function of the distance from the track (Fig. 8).

Between 0 and 12 μm distance from the penetration track the ratio of glial profiles was 0.16 ± 0.04 (area of glial elements ($μm^2$)/area of sector ($μm^2$)), which was significantly higher than the ratio in sectors between 48 and 180 μm distance from the penetration track (0.03 ± 0.02 in sector 168–180 μm). Between 12 and 24 μm the ratio of glial elements was still significantly increased (p < 0.05) compared to sectors at 168–180 μm from the track, although the value (0.09 ± 0.03)

was considerably lower than that in the sector of 0–12 μm.

From 24 μm distance onwards, the ratio of GFAP-positive elements dropped considerably and did not show any change up to 180 μm (Fig. 8) (for values, see Table 5). Importantly, the examination at the ultrastructural level indicated that despite the largely increased gliosis seen at light microscopic level, astroglial elements occupied only 16% of the neuropil even in the closest neighborhood of the implant.

4. Discussion

In this study we examined the long-term biocompatibility of the SU-8 material in the central nervous system with detailed quantitative methods. Our approach is based on a large sample size involving not only light- but also electron microscopic examinations. We examined two aspects of biocompatibility of key importance: 1) the preservation of neurons and synaptic contacts near the implant, which is important to obtain high quality neuronal signals; 2) the severity of the astrogliosis – which is responsible for the degradation of the electrical signal by sealing the implant from the brain.

Though SU-8 is widely used in the development of various neural implants [23,32,48,49] a detailed, in vivo, chronic, quantitative study
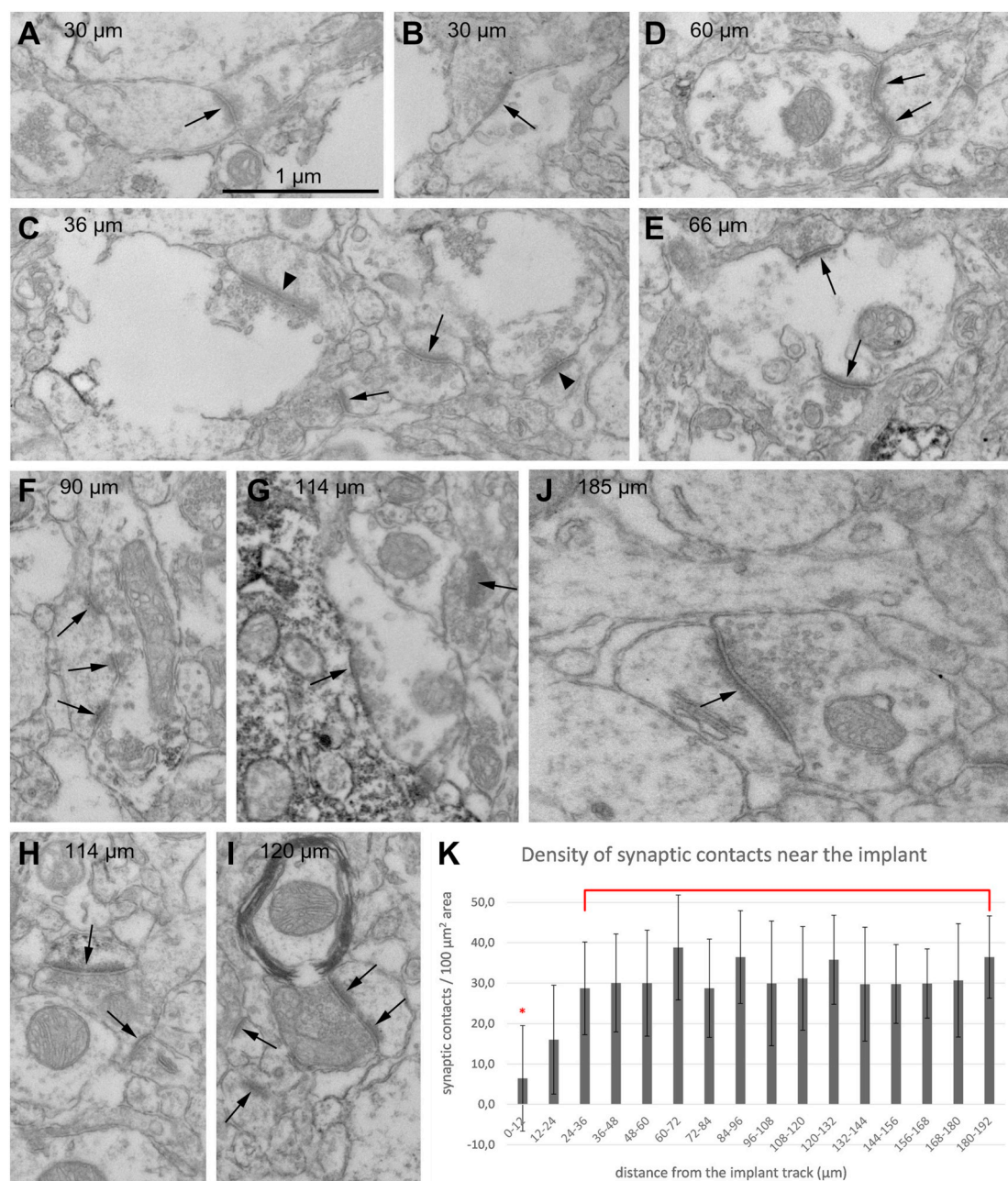
Fig. 7. High magnification electron micrographs showing synaptic contacts (arrows) at different distances from the penetration track. Large amounts of synaptic contacts could be found as close as 30 μm from the SU-8 implant (**A-C**). In some cases, especially closer to the track, the membranes of the pre- and/or postsynaptic elements were discontinuous, but the synaptic cleft seemed to be preserved (**C**, arrowheads). Synaptic contacts at larger distances were characterized by a healthy ultrastructure with intact pre- and postsynaptic profiles (**D-I**).

The quantification of the synaptic density near the implant was performed at the electron microscopic level (K). Synapses were counted in the neuropil and synaptic density was calculated as a function of the distance from the device track up to 192 μm distance. The first synapses appeared at a distance between 0 and 12 μm. However, the synaptic density was significantly reduced in this sector, compared to larger distances. From 24 μm the density of synaptic contacts did not show any significant changes compared to control regions. The asterisk labels significant difference, $p < 0.05$ (K).

of its biocompatibility on a high sample size, involving a detailed ultrastructural examination has not been performed yet in the CNS. These chronic in vivo investigations are indispensable to gain knowledge about the interaction between the material and the brain tissue. The safe use of the electrode material has to be proven in animal models before the development of devices for possible human use.

To analyze the neuronal loss and the severity of the astrogliosis in a quantitative manner, we developed and validated a cell counting and staining intensity assessing routine suitable to analyze a large number of light micrographs with high reliability.

The long term biofunctionality of an implanted device can be affected by multiple factors, such as mechanical effects (insertion procedure, then micromotions within the soft brain); foreign body reactions with subsequent inflammation and encapsulation of the implant and chronic neurodegeneration surrounding it.

The favorable mechanical properties of SU-8 devices has been demonstrated [19,31,50], showing that SU-8 is stiff enough to sustain resistance from brain tissue during implantation, but devices also remain flexible enough to prevent damage of the surrounding area.

Also, the viability of cells (including neurons) on SU-8 surfaces has

Table 4

Density of the synaptic contacts as a function of the distance from the SU-8 implant. The asterisk (*) labels significant difference compared to the other ROIs, $p < 0.05$.

Distance from the track (µm)	Number of synaptic contacts/ 100 µm area	StDev
0–12 *	6.44	13.05
12–24	16.01	13.47
24–36	28.74	11.47
36–48	30.06	12.13
48–60	30.02	13.12
60–72	38.84	13.00
72–84	28.74	12.17
84–96	36.47	11.49
96–108	29.95	15.43
108–120	31.20	12.83
120–132	35.79	11.01
132–144	29.76	14.10
144–156	29.80	9.75
156–168	29.90	8.56
168–180	30.70	14.03
180–192	36.45	10.19

been tested in several in vitro cell culture models showing no cytotoxicity and a good preservation of cells on the surface. Even the physiological state of cultured primary neurons was investigated by patch-clamp recordings by Matarése and colleagues [51]. The non-irritant nature of SU-8 was proven in muscle and subcutaneous implantations [10,29,30] and promising results were shown in brain applications as well [24,31,32]. However, despite the absence of cytotoxicity, alterations in gene expressions were found on certain SU-8 surfaces [52], which may influence the viability of cells in long-term chronic applications.

In addition, the investigation of the submicron interface between the implant and the neural tissue at the ultrastructural level is of key interest for a better understanding of the long-term reaction of living biological tissues to an artificial implant, no matter how apparently inert the material is [53].

Here we prove for the first time that SU-8 meets all requirements of long-term biocompatibility in CNS applications.

4.1. Neuronal survival neighboring SU-8 implants

Failure of chronic recording in long-term applications is a well-known and undesired phenomenon [54–57]. It was shown to be mainly connected to chronic inflammation caused by the constant presence of the device and the subsequent loss (degeneration) of the nearby neuronal population [58–60].

Simultaneous intra- and extracellular recordings from single neurons proved that the most reliable cluster separation of single units could be achieved when neurons were present within a 50 µm radius around the recording surface [61]. Therefore, preservation of neurons within this region is particularly important.

In this study we showed the long-term preservation of neurons near the SU-8 device in those cases where no injuries or bleedings occurred. An intense cell loss could be observed only in close vicinity of the penetration track, within 20 µm. Between 20 and 40 µm already 74% of neurons were preserved, whereas from 40 µm onwards, the neuronal density was control-like. Electron microscopic examination proved that synaptic contacts were present as close as 6–12 µm from the track and the density of synapses recovered to the control level as close as 24 µm from the track.

The favorable preservation of neurons and synaptic contacts observed in this study may suggest that SU-8 is a suitable material for maintaining long-term stable recordings from neurons in in vivo applications.
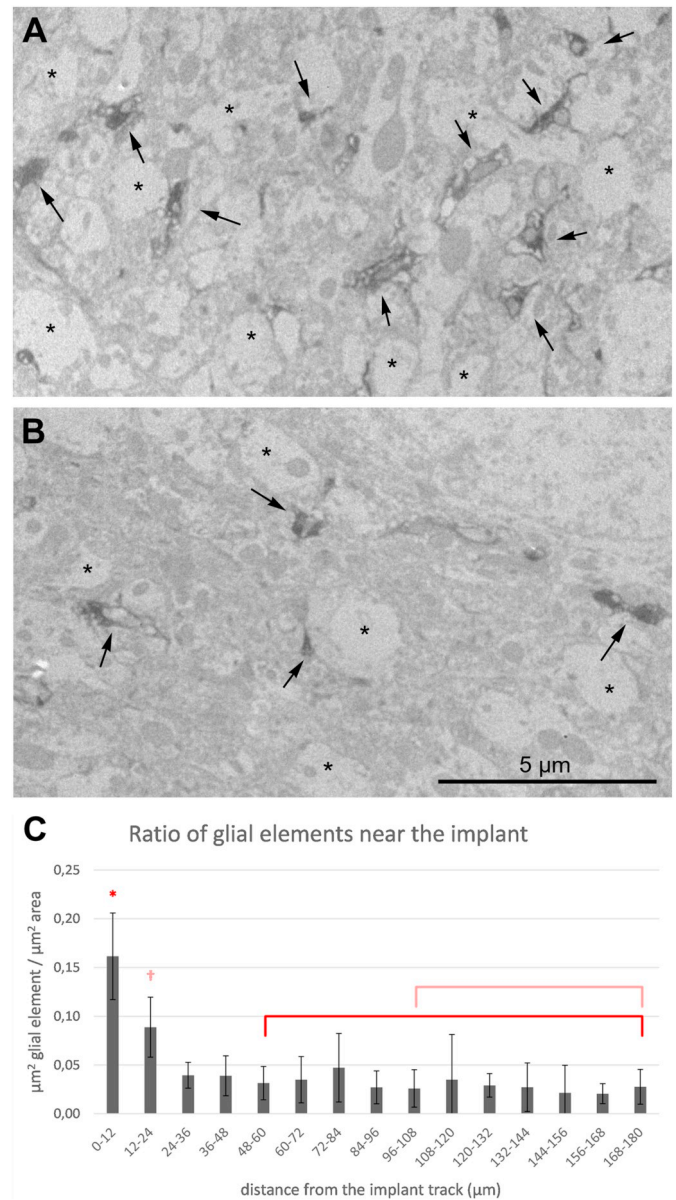

Fig. 8. Electron microscopic examination of the GFAP-positive elements surrounding the SU-8 implant. A: Up to 24 µm distance from the track, several GFAP-positive elements were visible (arrows), together with many caverns (asterisk) indicating tissue damage. B: At a larger distance (80 µm) the number of GFAP-immunostained elements was markedly decreased. C: A quantitative examination of the GFAP-positive glial elements as a function of the distance from the implant track was performed at the electron microscopic level.

Between a distance of 0–12 µm and 12–24 µm, significantly more glial profiles were found than at a distance from 48 µm to 96 µm, respectively. Note, that even in close vicinity of the track, the astroglial elements occupied only 16% of the neuropil. The asterisk (*) labels significant difference compared to sectors between 48 and 180 µm, $p < 0.05$. The cross (†) labels a significant difference compared to sectors between 96 and 180 µm, $p < 0.05$.

4.2. Astroglial reaction surrounding SU-8 implants

It is known that the encapsulation reaction isolates the probe from neighboring neurons resulting in an electrical sealing between the probe and the nearby neurons while also increasing the distance between the recording surface and recorded nerve cells [5,35,46,47,54,62,63].

Although, to a lesser degree than neuronal cell loss, astroglial sheet

Table 5
Ratio of glial elements as a function of the distance from the SU-8 implant. The asterisk (*) labels significant difference compared to sectors between 48 and 180 μm, $p < 0.05$. The cross (†) labels significant difference compared to sectors between 96 and 180 μm, $p < 0.05$.

Distance from the track (μm)	Ratio of glial elements (μm² glial elements/μm² area)	StDev
0–12 *	0.16	0.04
12–24 †	0.09	0.03
24–36	0.04	0.01
36–48	0.04	0.02
48–60	0.03	0.02
60–72	0.03	0.02
72–84	0.05	0.04
84–96	0.03	0.02
96–108	0.03	0.02
108–120	0.03	0.05
120–132	0.03	0.01
132–144	0.03	0.02
144–156	0.02	0.03
156–168	0.02	0.01
168–180	0.03	0.02

formation also contributes to the long-term decline in recording performance of implanted devices, by increasing electrical impedance [59,64–66]. Beside their passive barrier effect to tissue-device communication (shielding effects), glial processes should also be considered as the active modulators of neuronal excitability, synaptic transmission and network activity (for review see [46]).

For this reason it is important to examine the astroglial reaction at a high resolution at the ultrastructural level when assessing the long-term biofunctionality of a device [47]. In case of our SU-8 probes, an approximately 5 μm thick layer of scar tissue was found near the implant. This is in accordance with the literature: scar tissue was rarely found to exceed 10–20 μm from the foreign body [37,47,67].

We found a considerably increased astroglial staining – observed in the light microscope – in close vicinity of the probe track, with a normalized staining intensity of 0.29 ± 0.14 (compared to 1.01 ± 0.03 in the control region). Despite of this increased GFAP-staining adjacent to the implant, the ultrastructural examination revealed that astroglial processes were sparsely dispersed, occupying only 16% of the neuropil in close vicinity of the implant (0–12 μm). At larger distances, the ratio of glial elements was lower than 5%. This discrepancy between the light and electron microscopic results can be explained by methodological procedures. The penetration of the immunohistochemical reagents into the brain tissue is strongest on the surface of the sample and decreases towards the middle of the slice. The borders of the probe track form a perpendicular surface to the two (lower and upper) surfaces of the section, and thus provide an additional stained tissue volume. This results in a darker background staining than in regions, where this extra surface is lacking. Thus, our results suggest that the considerable increase in astroglial staining seen in the light microscope is partly due to this optical phenomenon.

Our electron microscopic analysis indeed showed signs of a slight gliosis around the implanted device. Similarly low levels of gliosis were found in the vicinity of highly biocompatible silicon-based probes [37]. We suggest that this low amount of encapsulation and the sparse distribution of the glial processes around the probe might not have a strong shielding effect. A few articles – describing the impact of glial encapsulation on the recording quality by applying electrophysiological recordings and post hoc histological examinations on the same system – support this idea. Studies, investigating the relationship between recording quality and histology showed a negative correlation between astroglial density and signal quality in case of silicon probes [68,69]. McCreery and colleagues showed that action potential amplitudes depended on astroglial density within the first 80 um distance from the device surface [70]. In case of polyimide probes, cellular and network

activity were recorded regularly to monitor the temporal change of several features of the electrophysiological performance [5]. Stable single-unit and multi-unit activity were recorded for several weeks with the implanted depth probes. After a 13-week survival, a weak or moderate tissue reaction was found around the probe track. Based on our results and the aforementioned studies, we can assume that the recording capability of the SU-8 device might lead to high quality recordings even in long-term applications.

Light microscopic examination revealed a significantly elevated astroglial staining intensity up to a distance of 480–560 μm from the device interface. Previous studies, including ours, describe similar results in case of silicon and various structured surfaces [35,37,58]. This suggests that the extent of the astroglial reaction may depend more on the mechanical trauma and less on the quality of the surface material or the topography itself [35,37]. Another finding also supports this idea. Both the intensity and the extension of the astroglial reaction close to the implant track were most enhanced in the upper layers of the neocortex, with a gradual decline towards the lower layers. This might be related to the higher amount and size of the blood vessels in the supragranular layers [37,71], which increases the chances of their injury during the insertion procedure. Disruption of the blood brain barrier is therefore more likely in the upper layers and can lead to an enhanced gliosis [46].

4.3. Comparing SU-8 implants to silicon probes

The highly biocompatible nature of silicon in long-term in vivo applications was shown by a large number of studies [35,37,58,72]. Therefore, we attempt to compare our findings with biocompatibility studies using silicon-based electrodes. Here we show that our SU-8 probes bear a similarly good biocompatible nature in chronic in vivo environments as it was shown for silicon devices.

Both the thickness of the glial scar and the extent of astroglial activation were comparable [35,37,47,58,67]. Similarly, the amount of glial processes in the vicinity of the probe was low in case of both materials [34,37]. The preservation of synaptic contacts was similarly propitious as for silicon devices [37,47].

Studies examining the biocompatibility of silicon based devices show a decreased neuronal survival typically up to 50–200 μm [35,37,58,73] and neuronal numbers were rarely shown to be recovered closer than 50 μm [72]. Our results, i.e. a neuronal density at 40–60 μm from the track which was control-like, indicate that the SU-8 material enables a better neuronal survival in close vicinity of the implant. This might be explained – beside good surface-chemistry parameters – by the more flexible nature of the SU-8 material, which enables a better mechanical coupling with the soft brain tissue [12,13,31].

For these reasons SU-8-based probes can be promising objects for the development of clinically adaptable devices.

4.4. Damages

In some cases, major or minor injuries and/or bleeding caused lesions were seen surrounding the penetration track. These damages may result either from the bleedings during the implantation procedure or from the mechanical stress caused by the movement of the device in later time points. Movements can be small micro motions of the brain or larger lateral excursion of the device.

To attenuate the initial penetrating injury, minimizing the neurovascular damage is of key importance. Kozai and colleagues offer an effective method, using two-photon microscopy mapping during insertion of the microelectrode [74]. They emphasize that the foreign body response is considerably higher when a single major cortical artery was hurt compared with penetrating through many small capillaries.

Insertion speed may also be a crucial factor. Advancing rigid probes slowly into the brain can be more advantageous by providing the

surrounding tissue time to accommodate [36,75]. Lower tissue damage and a larger number of separable single units were found after slow insertion speeds (2 μm/s), compared to fast ones (20 μm/s – 1 mm/s) [36]. However, the optimal insertion speed in case of the more flexible SU-8 devices has yet to be investigated.

Trying to prevent later movements of the probe brings up the question of the fixation technique of the device. According to the literature, tethered implants evoke a larger tissue reaction than untethered ones, with a significantly larger astrocytic response [76,77] and reduced neuronal staining [76].

Injuries or lesions were more frequent and severe in the superficial layers. This is probably also connected to the higher number and larger area of the blood vessels towards the apical surface of the neocortex [37,71].

5. Conclusions

Studies on the long-term viability of implanted devices are essential both in the case of basic research and for future clinical applications. Here, we studied the chronic in vivo biocompatibility of SU-8 implants in the CNS, providing quantitative data on a large sample size.

Biocompatibility within a 50 μm radius around the recording surface is crucial to achieve good electrical signals [61]. A good neuronal preservation could be observed as close as 20–40 μm from SU-8 implants while the density of synapses recovered to the control level as close as 24 μm from the implant track. These results suggest that the SU-8 material provides the possibility of achieving good neuronal signals. Performing an electron microscopic examination as well, we have shown that the thickness of the glial scar was altogether 5–10 μm and the amount of glial processes in the neuropil was not >16% in the close proximity to the implant (0–12 μm), and that the latter dropped below 5% at a distance above 24 μm.

We can conclude, that in accordance with previous studies performed in cell culture models [10,20], and during muscle- [10] and subcutaneous implantations [29,30], SU-8 is biocompatible in the central nervous system as well. However, a reduction of the neurovascular damage by improving the surgical technique, avoiding large blood vessels during insertion and minimizing bleedings is of key importance to achieve good neuronal survival [74].

Due to its low-cost fabrication and more flexible nature, SU-8 based devices may offer an alternative to highly biocompatible silicon devices in future clinical applications.

Supplementary data to this article can be found online at https://doi.org/10.1016/j.msec.2020.110870.

Data availability

The raw/processed data required to reproduce these findings cannot be shared at this time due to technical limitations.

CRediT authorship contribution statement

Gergely Márton: Software, Investigation, Writing - original draft, Funding acquisition.**Estilla Zsófia Tóth:**Investigation, Formal analysis.**Lucia Wittner:**Resources, Writing - review & editing, Funding acquisition.**Richárd Fiáth:**Investigation, Validation, Writing - review & editing, Funding acquisition.**Domonkos Pinke:**Software, Visualization.**Gábor Orbán:**Methodology, Data curation.**Domokos Meszéna:**Investigation, Formal analysis.**Ildikó Pál:**Investigation, Visualization.**Edit Lelle Győri:**Investigation, Visualization.**Zsófia Bereczki:**Investigation, Data curation.**Ágnes Kandrács:** Investigation, Project administration.**Katharina T. Hofer**: Investigation, Data curation.**Anita Pongrácz:**Methodology, Funding acquisition.**István Ulbert:**Conceptualization, Supervision, Funding acquisition.**Kinga Tóth:**Methodology, Investigation, Writing - original draft, Project administration, Funding acquisition.

Declaration of competing interest

The authors declare that they have no known competing financial interests or personal relationships that could have appeared to influence the work reported in this paper.

References

[1] R. Fiáth, P. Beregszászi, D. Horváth, L. Wittner, A.A.A. Aarts, P. Ruther, H.P. Neves, H. Bokor, L. Acsády, I. Ulbert, Large-scale recording of thalamocortical circuits: in vivo electrophysiology with the two-dimensional electronic depth control silicon probe, J. Neurophysiol. 116 (2016) 2312–2330, https://doi.org/10.1152/jn.00318.2016.

[2] R. Fiáth, B.C. Raducanu, S. Musa, A. Andrei, C.M. Lopez, C. van Hoof, P. Ruther, A. Aarts, D. Horváth, I. Ulbert, A silicon-based neural probe with densely-packed low-impedance titanium nitride microelectrodes for ultrahigh-resolution in vivo recordings, Biosens. Bioelectron. 106 (2018) 86–92, https://doi.org/10.1016/j.bios.2018.01.060.

[3] R. Fiáth, B.C. Raducanu, S. Musa, A. Andrei, C.M. Lopez, M. Welkenhuysen, P. Ruther, A. Aarts, I. Ulbert, Fine-scale mapping of cortical laminar activity during sleep slow oscillations using high-density linear silicon probes, J. Neurosci. Methods 316 (2019) 58–70, https://doi.org/10.1016/j.jneumeth.2018.08.020.

[4] A.B. Schwartz, X.T. Cui, D.J. Weber, D.W. Moran, Brain-controlled interfaces: movement restoration with neural prosthetics, Neuron 52 (2006) 205–220, https://doi.org/10.1016/j.neuron.2006.09.019.

[5] R. Fiáth, K.T. Hofer, V. Csikós, D. Horváth, T. Nánási, K. Tóth, F. Pothof, C. Böhler, M. Asplund, P. Ruther, I. Ulbert, Long-term recording performance and biocompatibility of chronically implanted cylindrically-shaped, polymer-based neural interfaces, Biomed. Eng./Biomed. Tech. 63 (2018) 301–315, https://doi.org/10.1515/bmt-2017-0154.

[6] G. Buzsáki, Theta oscillations in the hippocampus, Neuron 33 (2002) 325–340, https://doi.org/10.1016/S0896-6273(02)00586-X.

[7] R. Csercsa, B. Dombovári, D. Fabó, L. Wittner, L. Eross, L. Entz, A. Sólyom, G. Rásonyi, A. Szucs, A. Kelemen, R. Jakus, V. Juhos, L. Grand, A. Magony, P. Halász, T.F. Freund, Z. Maglóczky, S.S. Cash, L. Papp, G. Karmos, E. Halgren, I. Ulbert, Laminar analysis of slow wave activity in humans, Brain 133 (2010) 2814–2829, https://doi.org/10.1093/brain/awq169.

[8] B. Wodlinger, J.E. Downey, E.C. Tyler-Kabara, A.B. Schwartz, M.L. Boninger, J.L. Collinger, Ten-dimensional anthropomorphic arm control in a human brain−machine interface: difficulties, solutions, and limitations, J. Neural Eng. 12 (2015) 016011, , https://doi.org/10.1088/1741-2560/12/1/016011.

[9] A.M. Dymond, L.E. Kaechele, J.M. Jurist, P.H. Crandall, Brain tissue reaction to some chronically implanted metals, J. Neurosurg. 33 (1970) 574–580, https://doi.org/10.3171/jns.1970.33.5.0574.

[10] G. Kotzar, M. Freas, P. Abel, A. Fleischman, S. Roy, C. Zorman, J.M. Moran, J. Melzak, Evaluation of MEMS materials of construction for implantable medical devices, Biomaterials 23 (2002) 2737–2750, https://doi.org/10.1016/S0142-9612(02)00007-8.

[11] A. Zátonyi, G. Orbán, R. Modi, G. Márton, D. Meszéna, I. Ulbert, A. Pongrácz, M. Ecker, W.E. Voit, A. Joshi-Imre, Z. Fekete, A softening laminar electrode for recording single unit activity from the rat hippocampus, Sci. Rep. 9 (2019) 2321, https://doi.org/10.1038/s41598-019-39835-6.

[12] C. Hassler, T. Boretius, T. Stieglitz, Polymers for neural implants, J. Polym. Sci. Part B Polym. Phys. 49 (2011) 18–33, https://doi.org/10.1002/polb.22169.

[13] T.D.Y. Kozai, A.S. Jaquins-Gerstl, A.L. Vazquez, A.C. Michael, X.T. Cui, Brain tissue responses to neural implants impact signal sensitivity and intervention strategies, ACS Chem. Neurosci. 6 (2015) 48–67, https://doi.org/10.1021/cn500256e.

[14] K. Wang, C.-C. Liu, D.M. Durand, Flexible nerve stimulation electrode with iridium oxide sputtered on liquid crystal polymer, IEEE Trans. Biomed. Eng. 56 (2009) 6–14, https://doi.org/10.1109/TBME.2008.926691.

[15] D. Simon, T. Ware, R. Marcotte, B.R. Lund, D.W. Smith, M. Di Prima, R.L. Rennaker, W. Voit, A comparison of polymer substrates for photolithographic processing of flexible bioelectronics, Biomed. Microdevices 15 (2013) 925–939, https://doi.org/10.1007/s10544-013-9782-8.

[16] A. del Campo, C. Greiner, SU-8: a photoresist for high-aspect-ratio and 3D submicron lithography, J. Micromech. Microeng. 17 (2007) R81–R95, https://doi.org/10.1088/0960-1317/17/6/r01.

[17] S. Keller, G. Blagoi, M. Lillemose, D. Haefliger, A. Boisen, Processing of thin SU-8 films, J. Micromech. Microeng. 18 (2008) 125020, , https://doi.org/10.1088/0960-1317/18/12/125020.

[18] R. Martinez-Duarte, M.J. Madou, SU-8 photolithography and its impact on microfluidics, in: S. Chrakaborthy, S.K. Mitra (Eds.), Microfluidics and Nanofluidics Handbook: Fabrication, Implementation and Applications, CRC Press, 2011, pp. 231–268, , https://doi.org/10.1201/b11188-11.

[19] A. Altuna, G. Gabriel, L. Menendez de la Prida, M. Tijero, A. Guimera, J. Berganzo, R. Salido, R. Villa, L.J. Fernandez, SU-8-based microneedles for in vitro neural applications, J. Micromech. Microeng. 20 (2010) 064014, , https://doi.org/10.1088/0960-1317/20/6/064014.

[20] S.-H. Cho, H.M. Lu, L. Cauller, M.I. Romero-Ortega, J.-B. Lee, G.A. Hughes, Biocompatible SU-8-based microprobes for recording neural spike signals from regenerated peripheral nerve fibers, IEEE Sensors J. 8 (2008) 1830–1836, https://doi.org/10.1109/JSEN.2008.2006261.

[21] F. Ejserholm, P. Köhler, M. Bengtsson, H. Jörntell, J. Schouenborg, L. Wallman, A polymer based electrode array for recordings in the cerebellum, 5th International IEEE/EMBS Conference on Neural Engineering (NER). IEEE, 2011, pp. 376–379, , https://doi.org/10.1109/NER.2011.5910565.

[22] G. Márton, M. Kiss, G. Orbán, A. Pongrácz, I. Ulbert, A polymer-based spiky microelectrode array for electrocorticography, Microsyst. Technol. 21 (2015) 619–624, https://doi.org/10.1007/s00542-014-2203-y.

[23] A. Altuna, E. Bellistri, E. Cid, P. Aivar, B. Gal, J. Berganzo, G. Gabriel, A. Guimerà, R. Villa, L.J. Fernández, L. Menendez de la Prida, SU-8 based microprobes for simultaneous neural depth recording and drug delivery in the brain, Lab Chip 13 (2013) 1422–1430, https://doi.org/10.1039/c3lc41364k.

[24] L.J. Fernandez, A. Altuna, M. Tijero, G. Gabriel, R. Villa, M.J. Rodriguez, M. Batlle, R. Vilares, J. Berganzo, F.J. Blanco, Study of functional viability of SU-8-based microneedles for neural applications, J. Micromech. Microeng. 19 (2009) 025007, , https://doi.org/10.1088/0960-1317/19/2/025007.

[25] B. Beche, N. Pelletier, E. Gaviot, Single-mode TE00–TM00 optical waveguides on SU-8 polymer, Opt. Commun. 230 (2004) 91–94, https://doi.org/10.1016/j.optcom.2003.11.016.

[26] B. Rubehn, S.B.E. Wolff, P. Tovote, M. Schuettler, A. Lüthi, T. Stieglitz, Polymer-based shaft microelectrodes with optical and fluidic capabilities as a tool for optogenetics, IEEE Engineering in Medicine and Biology Society (2011) 2969–2972, https://doi.org/10.1109/IEMBS.2011.6090815.

[27] M. Hennemeyer, F. Walther, S. Kerstan, K. Schürzinger, A.M. Gigler, R.W. Stark, Cell proliferation assays on plasma activated SU-8, Microelectron. Eng. 85 (2008) 1298–1301, https://doi.org/10.1016/j.mee.2008.01.026.

[28] V.N. Vernekar, D.K. Cullen, N. Fogleman, Y. Choi, A.J. García, M.G. Allen, G.J. Brewer, M.C. LaPlaca, SU-8 2000 rendered cytocompatible for neuronal bioMEMS applications, J. Biomed. Mater. Res. Part A. (2009), https://doi.org/10.1002/jbm.a.31839.

[29] K.V. Nemani, K.L. Moodie, J.B. Brennick, A. Su, B. Gimi, In vitro and in vivo evaluation of SU-8 biocompatibility, Mater. Sci. Eng. C 33 (2013) 4453–4459, https://doi.org/10.1016/j.msec.2013.07.001.

[30] G. Voskerician, M.S. Shive, R.S. Shawgo, H. von Recum, J.M. Anderson, M.J. Cima, R. Langer, Biocompatibility and biofouling of MEMS drug delivery devices, Biomaterials 24 (2003) 1959–1967, https://doi.org/10.1016/S0142-9612(02)00565-3.

[31] S.-H. Huang, S.-P. Lin, J.-J.J. Chen, In vitro and in vivo characterization of SU-8 flexible neuroprobe: from mechanical properties to electrophysiological recording, Sensors Actuators A Phys. 216 (2014) 257–265, https://doi.org/10.1016/j.sna.2014.06.005.

[32] J. Liu, T.-M. Fu, Z. Cheng, G. Hong, T. Zhou, L. Jin, M. Duvvuri, Z. Jiang, P. Kruskal, C. Xie, Z. Suo, Y. Fang, C.M. Lieber, Syringe-injectable electronics, Nat. Nanotechnol. 10 (2015) 629–636, https://doi.org/10.1038/nnano.2015.115.

[33] J.C. Williams, M.M. Holecko, S.P. Massia, P. Rousche, D.R. Kipke, Multi-site incorporation of bioactive matrices into MEMS-based neural probes, J. Neural Eng. 2 (2005) L23–L28, https://doi.org/10.1088/1741-2560/2/4/L03.

[34] E. Azemi, C.F. Lagenaur, X.T. Cui, The surface immobilization of the neural adhesion molecule L1 on neural probes and its effect on neuronal density and gliosis at the probe/tissue interface, Biomaterials 32 (2011) 681–692, https://doi.org/10.1016/j.biomaterials.2010.09.033.

[35] Z. Bérces, K. Tóth, G. Márton, I. Pál, B. Kováts-Megyesi, Z. Fekete, I. Ulbert, A. Pongrácz, Neurobiochemical changes in the vicinity of a nanostructured neural implant, Sci. Rep. 6 (2016) 35944, , https://doi.org/10.1038/srep35944.

[36] R. Fiáth, A.L. Márton, F. Mátyás, D. Pinke, G. Márton, K. Tóth, I. Ulbert, Slow insertion of silicon probes improves the quality of acute neuronal recordings, Sci. Rep. 9 (2019) 111, https://doi.org/10.1038/s41598-018-36816-z.

[37] L. Grand, L. Wittner, S. Herwik, E. Göthelid, P. Ruther, S. Oscarsson, H. Neves, B. Dombovári, R. Csercsa, G. Karmos, I. Ulbert, Short and long term

[38] C.L. Kolarcik, D. Bourbeau, E. Azemi, E. Rost, L. Zhang, C.F. Lagenaur, D.J. Weber, X.T. Cui, In vivo effects of L1 coating on inflammation and neuronal health at the electrode-tissue interface in rat spinal cord and dorsal root ganglion, Acta Biomater. 8 (2012) 3561–3575, https://doi.org/10.1016/j.actbio.2012.06.034.

[39] L. Grand, A. Pongrácz, É. Vázsonyi, G. Márton, D. Gubán, R. Fiáth, B.P. Kerekes, G. Karmos, I. Ulbert, G. Battistig, A novel multisite silicon probe for high quality laminar neural recordings, Sensors Actuators A Phys. 166 (2011) 14–21, https://doi.org/10.1016/j.sna.2010.12.019.

[40] S. Beucher, F. Meyer, Segmentation: the watershed transformation. Mathematical morphology in image processing, Opt. Eng. 34 (1993) 433–481.

[41] E. Gould, A.J. Reeves, M.S.A. Graziano, C.G. Gross, Neurogenesis in the neocortex of adult primates, Science 286 (1999) 548–552, https://doi.org/10.1126/science.286.5439.548 (80-.).

[42] R.J. Mullen, C.R. Buck, A.M. Smith, NeuN, a neuronal specific nuclear protein in vertebrates, Development 116 (1992) 201–211.

[43] M. Kalman, F. Hajos, Distribution of glial fibrillary acidic protein (GFAP)-immunoreactive astrocytes in the rat brain - I, Forebrain. Exp. Brain Res. 78 (1989) 147–163.

[44] S. Ramón y Cajal, Histologie du système nerveux de l'homme & des vertébrés, Maloine, Paris, 1909, https://doi.org/10.5962/bhl.title.48637.

[45] M.V. Sofroniew, H.V. Vinters, Astrocytes: biology and pathology, Acta Neuropathol. 119 (2010) 7–35, https://doi.org/10.1007/s00401-009-0619-8.

[46] J.W. Salatino, K.A. Ludwig, T.D.Y. Kozai, E.K. Purcell, Glial responses to implanted electrodes in the brain, Nat. Biomed. Eng. 1 (2017) 862–877, https://doi.org/10.1038/s41551-017-0154-1.

[47] R.L. Schultz, T.J. Willey, The ultrastructure of the sheath around chronically implanted electrodes in brain, J. Neurocytol. 5 (1976) 621–642, https://doi.org/10.1007/BF01181577.

[48] A. Altuna, J. Berganzo, L.J. Fernández, Polymer SU-8-based microprobes for neural recording and drug delivery, Front. Mater. 2 (2015) 47, https://doi.org/10.3389/fmats.2015.00047.

[49] T.G. Schuhmann, T. Zhou, G. Hong, J.M. Lee, T.-M. Fu, H.-G. Park, C.M. Lieber, Syringe-injectable mesh electronics for stable chronic rodent electrophysiology, J. Vis. Exp. (2018), https://doi.org/10.3791/58003.

[50] H. Lorenz, M. Despont, N. Fahrni, N. LaBianca, P. Renaud, P. Vettiger, SU-8: a low-cost negative resist for MEMS, J. Micromech. Microeng. 7 (1997) 121–124, https://doi.org/10.1088/0960-1317/7/3/010.

[51] B.F.E. Matarèse, P.L.C. Feyen, A. Falco, F. Benfenati, P. Lugli, J.C. deMello, Use of SU8 as a stable and biocompatible adhesion layer for gold bioelectrodes, Sci. Rep. 8 (5560) (2018), https://doi.org/10.1038/s41598-018-21755-6.

[52] M. Stangegaard, Z. Wang, J.P. Kutter, M. Dufva, A. Wolff, Whole genome expression profiling using DNA microarray for determining biocompatibility of polymeric surfaces, Mol. BioSyst. 2 (2006) 421, https://doi.org/10.1039/b608239d.

[53] C. Marin, E. Fernández, Biocompatibility of intracortical microelectrodes: current status and future prospects, Front. Neuroeng. 3 (2010) 8, https://doi.org/10.3389/fneng.2010.00008.

[54] X. Liu, D.B. McCreery, R.R. Carter, L.A. Bullara, T.G. Yuen, W.F. Agnew, Stability of the interface between neural tissue and chronically implanted intracortical microelectrodes, IEEE Trans. Rehabil. Eng. 7 (1999) 315–326.

[55] M.A.L. Nicolelis, D. Dimitrov, J.M. Carmena, R. Crist, G. Lehew, J.D. Kralik, S.P. Wise, Chronic, multisite, multielectrode recordings in macaque monkeys, Proc. Natl. Acad. Sci. 100 (2003) 11041–11046, https://doi.org/10.1073/pnas.1934665100.

[56] P.J. Rousche, R.A. Normann, Chronic recording capability of the Utah intracortical electrode array in cat sensory cortex, J. Neurosci. Methods 82 (1998) 1–15, https://doi.org/10.1016/S0165-0270(98)00031-4.

[57] J.C. Williams, R.L. Rennaker, D.R. Kipke, Long-term neural recording characteristics of wire microelectrode arrays implanted in cerebral cortex, Brain Res. Brain Res. Protoc. 4 (1999) 303–313.

[58] R. Biran, D.C. Martin, P.A. Tresco, Neuronal cell loss accompanies the brain tissue response to chronically implanted silicon microelectrode arrays, Exp. Neurol. 195 (2005) 115–126, https://doi.org/10.1016/j.expneurol.2005.04.020.

[59] G.C. McConnell, H.D. Rees, A.I. Levey, C.-A. Gutekunst, R.E. Gross, R.V. Bellamkonda, Implanted neural electrodes cause chronic, local inflammation that is correlated with local neurodegeneration, J. Neural Eng. 6 (2009) 056003, , https://doi.org/10.1088/1741-2560/6/5/056003.

[60] B.D. Winslow, P.A. Tresco, Quantitative analysis of the tissue response to chronically implanted microwire electrodes in rat cortex, Biomaterials 31 (2010) 1558–1567, https://doi.org/10.1016/j.biomaterials.2009.11.049.

[61] D.A. Henze, Z. Borhegyi, J. Csicsvari, A. Mamiya, K.D. Harris, G. Buzsáki, Intracellular features predicted by extracellular recordings in the hippocampus in vivo, J. Neurophysiol. 84 (2000) 390–400, https://doi.org/10.1152/jn.2000.84.1.390.

[62] V.S. Polikov, P.A. Tresco, W.M. Reichert, Response of brain tissue to chronically implanted neural electrodes, J. Neurosci. Methods 148 (2005) 1–18, https://doi.org/10.1016/j.jneumeth.2005.08.015.

[63] J.N. Turner, W. Shain, D.H. Szarowski, M. Andersen, S. Martins, M. Isaacson, H. Craighead, Cerebral astrocyte response to micromachined silicon implants, Exp. Neurol. 156 (1999) 33–49, https://doi.org/10.1006/exnr.1998.6983.

[64] K.A. Ludwig, J.D. Uram, J. Yang, D.C. Martin, D.R. Kipke, Chronic neural recordings using silicon microelectrode arrays electrochemically deposited with a poly(3,4-ethylenedioxythiophene) (PEDOT) film, J. Neural Eng. 3 (2006) 59–70, https://doi.org/10.1088/1741-2560/3/1/007.

[65] D.R. Merrill, P.A. Tresco, Impedance characterization of microarray recording

electrodes in vitro, IEEE Trans. Biomed. Eng. 52 (2005) 1960–1965, https://doi.org/10.1109/TBME.2005.856245.

[66] R.J. Vetter, J.C. Williams, J.F. Hetke, E.A. Nunamaker, D.R. Kipke, Chronic neural recording using silicon-substrate microelectrode arrays implanted in cerebral cortex, IEEE Trans. Biomed. Eng. 51 (2004) 896–904, https://doi.org/10.1109/TBME.2004.826680.

[67] S. Schmidt, K. Horch, R. Normann, Biocompatibility of silicon-based electrode arrays implanted in feline cortical tissue, J. Biomed. Mater. Res. 27 (1993) 1393–1399, https://doi.org/10.1002/jbm.820271106.

[68] N.F. Nolta, M.B. Christensen, P.D. Crane, J.L. Skousen, P.A. Tresco, BBB leakage, astrogliosis, and tissue loss correlate with silicon microelectrode array recording performance, Biomaterials 53 (2015) 753–762, https://doi.org/10.1016/j.biomaterials.2015.02.081.

[69] E.K. Purcell, D.E. Thompson, K.A. Ludwig, D.R. Kipke, Flavopiridol reduces the impedance of neural prostheses in vivo without affecting recording quality, J. Neurosci. Methods 183 (2009) 149–157, https://doi.org/10.1016/j.jneumeth.2009.06.026.

[70] D. McCreery, S. Cogan, S. Kane, V. Pikov, Correlations between histology and neuronal activity recorded by microelectrodes implanted chronically in the cerebral cortex, J. Neural Eng. 13 (2016) 036012, , https://doi.org/10.1088/1741-2560/13/3/036012.

[71] T. Saxena, L. Karumbaiah, E.A. Gaupp, R. Patkar, K. Patil, M. Betancur, G.B. Stanley, R.V. Bellamkonda, The impact of chronic blood–brain barrier breach

on intracortical electrode function, Biomaterials 34 (2013) 4703–4713, https://doi.org/10.1016/j.biomaterials.2013.03.007.

[72] D.J. Edell, V.V. Toi, V.M. McNeil, L.D. Clark, Factors influencing the biocompatibility of insertable silicon microshafts in cerebral cortex, IEEE Trans. Biomed. Eng. 39 (1992) 635–643, https://doi.org/10.1109/10.141202.

[73] K.A. Moxon, S. Hallman, A. Aslani, N.M. Kalkhoran, P.I. Lelkes, Bioactive properties of nanostructured porous silicon for enhancing electrode to neuron interfaces, J. Biomater. Sci. Polym. Ed. 18 (2007) 1263–1281, https://doi.org/10.1163/156856207782177882.

[74] T.D.Y. Kozai, T.C. Marzullo, F. Hooi, N.B. Langhals, A.K. Majewska, E.B. Brown, D.R. Kipke, Reduction of neurovascular damage resulting from microelectrode insertion into the cerebral cortex using in vivo two-photon mapping, J. Neural Eng. 7 (2010) 046011, , https://doi.org/10.1088/1741-2560/7/4/046011.

[75] C.S. Bjornsson, S.J. Oh, Y.A. Al-Kofahi, Y.J. Lim, K.L. Smith, J.N. Turner, S. De, B. Roysam, W. Shain, S.J. Kim, Effects of insertion conditions on tissue strain and vascular damage during neuroprosthetic device insertion, J. Neural Eng. 3 (2006) 196–207, https://doi.org/10.1088/1741-2560/3/3/002.

[76] R. Biran, D.C. Martin, P.A. Tresco, The brain tissue response to implanted silicon microelectrode arrays is increased when the device is tethered to the skull, J. Biomed. Mater. Res. A 82 (2007) 169–178, https://doi.org/10.1002/jbm.a.31138.

[77] Y.-T. Kim, R.W. Hitchcock, M.J. Bridge, P.A. Tresco, Chronic response of adult rat brain tissue to implants anchored to the skull, Biomaterials 25 (2004) 2229–2237, https://doi.org/10.1016/j.biomaterials.2003.09.010.